Chem Catalysis

CellPress

Article

Highly durable fuel cell electrocatalyst with low-loading Pt-Co nanoparticles dispersed over single-atom Pt-Co-N-graphene nanofiber

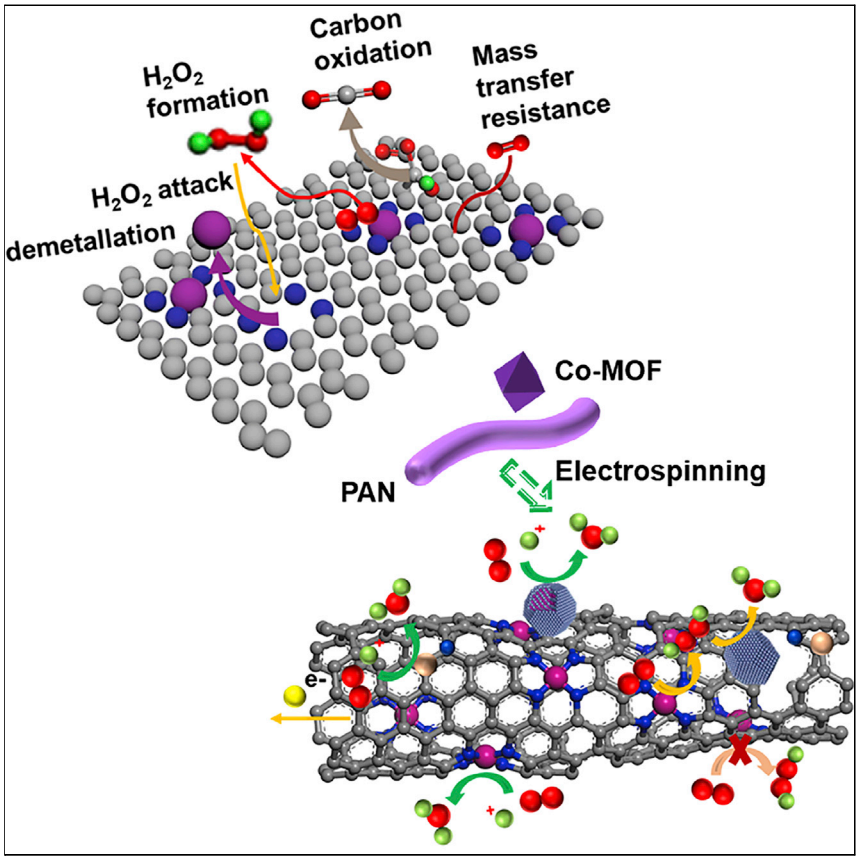

PtCo@Pt-Co-GNF catalyst is prepared via *in situ* reducing Pt over Co-N-graphene nanofiber obtained through electrospinning a solution containing Co metal-organic framework and polyacrylonitrile polymer as precursor. The catalyst delivers unprecedented catalytic activity and sustained durability toward oxygen reduction reaction under practical proton exchange membrane fuel cell (PEMFC), suggesting that it is a promising candidate for application in PEMFC.

Lina Chong, Hua Zhou, Joseph Kubal, ..., Hong Zhu, Jianxin Zou, Wenjiang Ding

chonglina@sjtu.edu.cn (L.C.)
jwen@anl.gov (J.W.)
jxzou@sjtu.edu.cn (J.Z.)

Highlights

PEMFC with ultra-low Pt loading could deliver high mass activity of 2.48 A mg_{Pt}^{-1}

PtCo@Pt-Co-GNF maintains 80% of initial activity after 60,000 AST cycles under PEMFC

H_2O_2 formation could be suppressed through enhancing the curvature of the substrate

The ORR activity of the Co site could be improved via local atomic structure engineering

Chong et al., Chem Catalysis 3, 100541
March 16, 2023
https://doi.org/10.1016/j.checat.2023.100541

Chem Catalysis

CellPress

Article

Highly durable fuel cell electrocatalyst with low-loading Pt-Co nanoparticles dispersed over single-atom Pt-Co-N-graphene nanofiber

Lina Chong,[1,4,7,*] Hua Zhou,[3] Joseph Kubal,[1] Qingli Tang,[5] Jianguo Wen,[2,*] Zhenzhen Yang,[1] Ira D. Bloom,[1] Daniel Abraham,[1] Hong Zhu,[5] Jianxin Zou,[4,6,*] and Wenjiang Ding[4,6]

SUMMARY

The limited durability of Pt electrocatalysis toward cathodic O_2 reduction reaction remains challenging, yet it is crucial for the development of proton exchange membrane fuel cells. Here, we present a rational design of a robust catalyst consisting of PtCo nanoparticles supported on Pt-Co-N-graphene nanofiber prepared through electrospun Co metal-organic framework. The catalyst delivers unprecedented mass activity of 2.48 $A \cdot mg_{Pt}^{-1}$ and retains 80% of initial value after 60,000 accelerated stress test cycles. *Operando* X-ray absorption spectroscopies show that the electronic configurations of Pt sites in PtCo and Co sites in Co-N_4 in the hybrid catalyst are modified toward high catalytic activities. Density functional theory shows that the enhanced curvature of the substrate induced by the morphology engineering lowers the reaction thermodynamic barrier on Co-N_4 sites, favoring the formation of H_2O and suppressing that of H_2O_2. This result, along with the strong affinity of PtCo nanoparticles to the Pt-Co-N-graphene fiber, endows the catalyst with exceptional durability.

INTRODUCTION

Proton exchange membrane fuel cells (PEMFCs) are considered as a promising high-efficiency, clean-energy technology having a theoretical specific energy sufficient for transportation and stationary applications.[1–3] The four-electron transferred oxygen reduction reaction (ORR) at the cathode is paramount for fuel cell operation, and its sluggish kinetics, which is six orders of magnitude lower than the hydrogen oxidation reaction at the anode, limits overall performance of the PEMFC.[3,4] The Pt usage of a commercial fuel-cell-powered vehicle is 30 g per stack, which is substantially higher than the 2–8 g_{Pt} in incumbent internal combustion engine (ICE) vehicles, and far from the long-term sustainability target of <5 g_{Pt} per vehicle.[5] To compete with ICE vehicles, the total Pt-group-metal (PGM) loading, including anode and cathode on the membrane electrode assembly (MEA), should be restricted to less than 0.125 $mg_{Pt}\ cm^{-2}$, giving 8 g of PGM per vehicle. Designing highly active, durable, and cost-effective electrocatalysts to boost ORR and reduce the Pt consumption without compromising performance in a fuel cell is challenging and critical for the widespread commercial application of PEMFCs.[3,6]

Remarkable progress has been made over the last decade in the development of low-loading PGM and PGM-free electrocatalysts synthesized from earth-abundant, cost-effective, and easily sourced materials. Regarding low-loading PGM catalyst, many of the research efforts are aimed at developing novel Pt-based nanoparticles

THE BIGGER PICTURE

Despite considerable accomplishments in the development of ultra-low-Pt-group metal (PGM) and PGM-free oxygen reduction reaction (ORR) catalysts for proton exchange membrane fuel cells (PEMFCs), great challenges still remain, among which is the instability of the membrane electrode assembly, which must be addressed before PEMFCs could be considered for a broad deployment. In addition, a hybrid catalyst that contains both PGM and PGM-free catalysts has been developed with high catalytic efficiency; however, the synergy and the relationship of structure-performance are not fully understood. This article describes a method of preparing a high-efficiency synergistic ORR catalyst, putting emphasis on its operating durability in PEMFCs. This work unravels the contribution associated with catalyst structure and features a facile scalability, representing rational designs of ultra-low-PGM and PGM-free efficient catalysts through structural regulation, including morphology engineering and local atomic structure innovation for sustainable energy application.

(NPs) with improved catalytic activities and durability toward ORR through forming alloys, tuning morphologies, and manipulating architectures.[7,8] Several concepts for Pt-based NP developments are present that exceed the US Department of Energy 2025 target set for Pt mass activity for ORR. Despite spectacular progress in low-loading PGM catalyst development for proton exchange membrane (PEM) fuel cells, such catalysts still suffer from metal dissolution,[9] particle agglomeration (especially for particle sizes below 3 nm), and C corrosion during an accelerated stress test (AST).[10] Moreover, there is still a wide gap to translate the intrinsic activity to MEA and practical fuel cells.[11] The commonly used support for such Pt-based NPs is commercial C black, which has weak PGM particle-support interaction and lack of anchoring sites for PGM particles, leading to an easy agglomeration of the PGM particles and accordingly a decrease in active-site density during AST. Additionally, automotive fuel cell systems operate at high current density where mass transfer becomes crucial,[12] and macro-pores as well as low O_2 transfer resistance are imperative.[13] Therefore, besides the development of novel PGM particles, rational design of C support for sustained high activity and stability of a catalyst for PEMFCs is pivotal and challenging.

Significant progress has also been achieved for PGM-free catalysts in recent years, and the initial activity of its MEA is approaching that of the commercial Pt/C at low Pt loading.[14] However, numerous challenges still remain before the PGM-free catalyst is viable for PEMFCs, of which the catalyst instability must be addressed. For example, the performance of PEMFCs having an Fe/Co-N-C PGM-free cathodic catalyst typically degrades by 40%–80% in the first 100 h of testing, far from meeting commercialization demands. Possible degradation mechanisms have been related to [10,15] (1) demetallation or C/N corrosion, (2) active site protonation causing anion adsorption, (3) peroxide oxidation, and (4) micropore flooding. The presence of peroxide/radical is considered detrimental to the stability of C and $M-N_4$ moieties.[10,16] However, PGM particles have catalytic ability to decompose H_2O_2.[4] To overcome the issues raised by the H_2O_2, coupling low-loading PGM NPs with PGM-free substrates could be a promising method for innovation of synergistic catalysts with improved catalytic activities and sustained durability for ORR. A hybrid catalyst with only 3 wt % of PtCo NPs over a Co-N-C substrate (LP@PF-1) was synthesized and achieved high Pt mass activity of 1.08 A mg_{Pt}^{-1}, and 64% retention of initial activity after 30,000 AST cycles.[4] The stability of this hybrid catalyst is far better than that of Co-N-C alone. A series of similar synergistic catalysts by using Cu metal-organic framework (MOF)- or NiCo zeolite-imidazole framework (ZIF)-derived C as support for high-efficiency and active low-loading Pt catalysts were successful synthesized.[17,18] In particular, a hybrid catalyst containing Pt_3Co supported on $Co-N_4$-decorated C fiber obtained through pyrolysis of ZIF67-based polymer fiber shows promising fuel cell performance at 160°C.[19] Despite this remarkable progress, compensating for the inability to achieve commercialization remains challenging, and tremendous efforts need to be dedicated to the reaction mechanism contributing to the significantly improved catalytic activity, as well as the complicated instability mechanism.

For development of an ideal catalyst with high initial activity and durability for ORR, the designed C as supporting material should be highly graphitized, hierarchical porous, high surface area, of rich loading sites, and have strong affinity to PGM particles. In addition, the reactants (O_2 and proton) and products (H_2O), should transfer directly to and out the micropores, where the active sites including the PGM and PGM-free moieties are densely populated. Moreover, when a fuel cell operates at relatively high overpotential in an automotive system, such as 0.6 V, high current

[1]Chemical Sciences and Engineering Division, Argonne National Laboratory, Argonne, IL 60439, USA

[2]Center for Nanoscale Materials, Argonne National Laboratory, Argonne, IL 60439, USA

[3]Advanced Photon Source, Argonne National Laboratory, Argonne, IL 60439, USA

[4]Hydrogen Energy Center, Key Laboratory of Shanghai, Material Science and Engineering division, Shanghai Jiao Tong University, Shanghai 200240, China

[5]University of Michigan, Joint Institute of Shanghai Jiao Tong University, Shanghai 200240, China

[6]National Engineering Research Center of Light Alloys Net Forming and State Key Laboratory of Metal Matrix Composite, Shanghai Jiao Tong University, Shanghai 200240, China

[7]Lead contact

*Correspondence: chonglina@sjtu.edu.cn (L.C.), jwen@anl.gov (J.W.), jxzou@sjtu.edu.cn (J.Z.)

https://doi.org/10.1016/j.checat.2023.100541

density is often reached, and mass transfer, especially O_2 resistance, becomes rate limiting.[12] It has been shown in previous research that the macro-pores play a crucial role in governing the effective mass transfer of both reactants and product to and from the active sites freely with minimal resistance throughout electrode layers. However, the dominant micropores (1–2 nm) and small mesopores (2–50 nm) of the C derived from pure MOF have significantly limited access of reactants to, and products away from, the active sites in the complicated MEA, which may cause severe mass transport and water flooding in the catalyst layers.[20] Nanofiber morphology is beneficial for mass transfer, which can be achieved by electrospinning.[21] In addition, electrospun MOF with a polymer carrier can enhance micro-porosity of the C nanofiber,[13] resulting in improved catalytic activity. Moreover, the macropore in between the entwined fibers promotes O_2 permeability, enabling high current production. On the other hand, the macropore functions as a water drain during PEMFC operation, mitigating water flooding. Last but not least, the fibrous backbone with homogeneous distribution of N-C and/or transition metal-N decorations not only facilitates uniform distributed ionomer coverage throughout the catalyst but also enhances the electron conductivity.[22] Therefore, it is feasible and pivotal to reasonably design and develop a highly graphitized 3D-structured C with high surface area and hierarchical porosity for integration with low-loading PGM NPs to obtain a synergistic hybrid catalyst with high activity and long-term stability for PEMFC.

In this work, we introduce a new design of a hybrid catalyst, where an ultra-low loading of PtCo NPs dispersed on the Pt-Co-graphene-N nanofiber (Pt-Co-GNF) prepared from electrospun polymer fiber containing Co-MOF. The Pt-Co-GNF possesses high surface area, hierarchical pore structure, and densely populated Co-N_4 moieties, as well as a trace amount of single-atomic Pt sites. Co-ZIF, a member of the MOF family, was selected for this study as the source of Co-N_4 active site formation.[23] Also, it served as the metallic Co source that was the nucleation center for further PtCo alloy synthesis.[4] We chose PtCo alloy because the ordered core@shell structured PtCo NP demonstrated balanced activity and stability among PGM NPs.[24] The PtCo@Pt-Co-GNF exhibits a high mass activity of 5.48 $\pm$ 0.41 A mg_{Pt}^{-1} measured in a rotating ring-disk electrode (RRDE) experiment, which is 246 and 15 times that of Pt/C and the state-of-the-art Pt_3Co/C(Um), respectively. In an H_2-O_2 PEMFC cell with total Pt loading (anode + cathode) of 0.083 mg_{Pt} cm^{-2}, PtCo@Pt-Co-GNF achieved unprecedented mass activity of 2.48 $\pm$ 0.18 A mg_{Pt}^{-1}, and Pt utilization of 11.9 $\pm$ 0.8 kW g_{Pt}^{-1} at 150 kPa_{abs}. The catalyst was highly stable, retaining 80% of initial mass activity after 60,000 cycles of AST, including 30,000 cycles in H_2-air and a continued 30,000 cycles in H_2-O_2 cell. The inherent high activity and exceptional durability of PtCo@Pt-Co-GNF toward ORR were systematically studied through *operando* X-ray absorption spectroscopy (XAS) experiments and density functional theory (DFT) calculation.

RESULTS AND DISCUSSION

Synthesis and characterization of PtCo@Pt-Co-GNF

Co-ZIF was first fabricated into interconnected nanofiber by electrospinning its mixture with polyacrylonitrile (PAN). PAN was selected as the sacrificial polymer carrier and graphene source, as it can be converted to n-type N-doped graphene possessing excellent electron conductivity, corrosion resistance, and mechanical strength through high-temperature pyrolysis.[25] Meanwhile, it offers additional N-functional groups that could facilitate the homogeneous distribution of ionomer throughout the catalyst layers, and provide anchoring sites for stabilization of

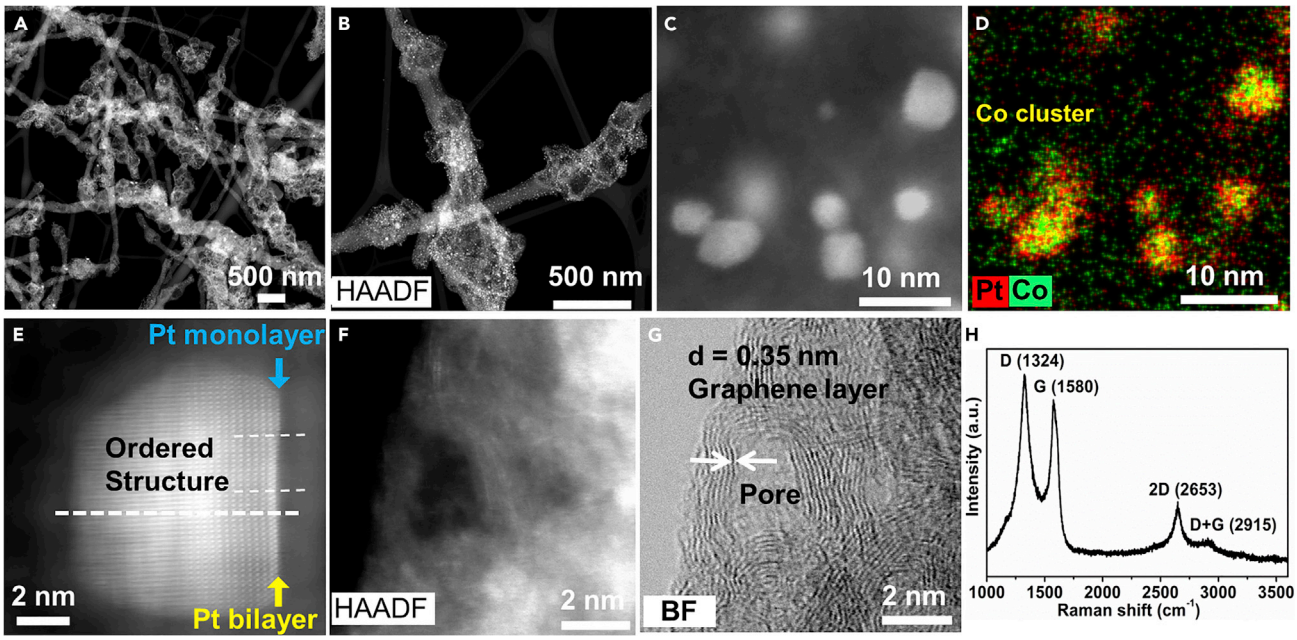

Figure 1. Morphology characterization of PtCo@Pt-Co-GNF

(A and B) HAADF-STEM images of fibrous PtCo@Pt-Co-GNF catalyst.

(C) HAADF-STEM image of PtCo alloy NPs in PtCo@Pt-Co-GNF.

(D) The corresponding EDS elemental mapping, Pt versus Co.

(E) Atomic-resolution Z-contrast HAADF-STEM image of a representative PtCo alloy NP, displaying ordered PtCo core and mono-/bilayer Pt shell.

(F and G) (F) Atomic-resolution HAADF-STEM image of C substrate, showing isolated single Co atoms distributed across the C surface. (G) The corresponding bright-field HRTEM of C substrate, showing curved thin graphene layer.

(H) Raman spectrum of PtCo@Pt-Co-GNF, showing the graphene nature of the C substrate.

Co/Pt atoms, maximizing efficiency of triple phase boundary (TPB).[26,27] Last but not least, it functions as pore-forming agent to form 3D interconnected hierarchical porous structure. The obtained fiber mat was subjected to heat treatment at 1,000°C for 1.5 h under flowing Ar atmosphere. After pre-leaching in 0.5 M H_2SO_4, the obtained material, denoted as Co-N-GF, was used as a support and nucleation center for the *in situ* reduced Pt cluster. A second heat treatment under NH_3 was performed as the final step of the catalyst synthesis (PtCo@Pt-Co-GNF). The synthesis process is schematically shown in Figure S1. The NH_3 was used as an additional N precursor, as NH_3 gasifies the disordered domains of the C, (1) creating micropores into the support; (2) producing N-bearing functionalities to bind Co cations, forming Co-N_x sites; (3) generating n-type graphene by donating electrons to graphene,[28] facilitating ORR.[29]

The catalyst has an interconnected network structure, with "beads" lining up on the "string" (Figures 1A and 1B; Figures S2B and S2C). The beads were converted from Co-ZIF, maintaining MOF-like morphology with hollowed structure. High-angle annular dark-field scanning transmission electron microscopy (HAADF-STEM) images, combined with energy-dispersive X-ray spectroscopy (EDS) elemental mapping, revealed the formation of PtCo alloy dispersed over the homogeneous atomic Co, N, and Pt decorated C matrix (Figures 1C and 1D; Figures S3A–S3D). The average particle size was 3.2 ± 1.3 nm (Figures S2D and S2E), including PtCo NP and metallic Co cluster (Figure 1D). Atomic-resolution Z-contrast HAADF-STEM image combined with line scanning profile and high-resolution TEM (HRTEM) image revealed that the PtCo alloy possessed a core-shell structure with mono-/bilayer

of Pt as shell and the ordered PtCo alloy as core (Figure 1E; Figures S3E–S3H; Figures S4 and S5). High-energy X-ray diffraction (XRD) further confirmed the formation of the ordered PtCo alloy (Figure S6A). The Pt-Co-GNF substrate prevented the particle size of PtCo from growing to a large size at high temperature, which may be ascribed to the thermodynamic stability of graphene and the strong affinity of PtCo to the Pt-Co-N anchoring site in the graphene matrix (Figures S6B and S6C). The average Pt/Co composition of 50/50 for PtCo alloy was confirmed by means of HADDF-STEM-EDS elemental analysis of over 100 PtCo particles (Figure S3G). The average atomic ratio of Co:N:Pt:C for PtCo@Pt-Co-GNF was 1.6:4.0:0.4:94 measured by HAADF-STEM-EDS (Figure S7). The Pt concentration of 4.8% $\pm$ 0.2 wt % was determined by inductively coupled plasma-optical emission spectrometry (ICP-OES). The Pt shell was strained and partially covered with Co-N_x/C terraces (Figure S5), which could protect Co/Pt against leaching under harsh operating conditions in the practical fuel cell.[4] Atomic-resolution HAADF-STEM further revealed the densely populated single-atomic Co/Pt sites embedded in the C matrix (Figures 1D and 1F). Electron energy-loss spectroscopy (EELS) demonstrated the co-existence of N with Co (Figure S8), suggesting Co-N_x populations.[30] Bright-field STEM images showed that the C mainly consisted of graphene sheets, with ~0.35-nm d-spacing of the (002) basal plane in both beads and string (Figure 1G; Figure S2F). This value is larger than the d-spacing of well-ordered graphite (0.34 nm), suggesting the incorporation of N into the graphitic structure and/or additional defect sites generated in the graphene matrix. Raman spectrum (Figure 1H) further confirmed the graphene nature of the C fiber as shown by the peaks at 2,653 cm^{-1} and 2,915 cm^{-1} corresponding to 2D band and D + G band of graphene,[31] respectively, attesting to the high degree of graphitization. The PtCo@Pt-Co-GNF achieved high surface areas of 701.4 m^2 g^{-1} (Figure S9A; Table S1), as determined by the Brunauer-Emmett-Teller (BET) method. The N adsorption measurement showed that the volumes of micropores and mesopores were ~0.48 and ~0.18 cm^3 g^{-1}, respectively, showing the predominant presence of micropores (Figure S9B). Co-electrospinning Co-MOF with PAN polymer carrier results in an increased micro-porosity of the obtained graphene nanofiber (Figures S13E and S13G). Jaouen et al. found that micropore was the primary factor governing the ORR catalytic activity.[32] Therefore, a high volumetric activity would be predicted for PtCo@Pt-Co-GNF.

We performed X-ray photoelectron spectroscopy (XPS) and XAS to elucidate the surface composition, oxidation states, and local atomic structure of PtCo@Pt-Co-GNF. The Pt XPS spectrum shows a 0.2 eV positive shift in binding energy after NH_3 annealing, relative to that of PtCo@Pt-Co-GNF before NH_3 treatment (PtCo@Pt-Co-GNF-BN, Figure 2A), suggesting an electron transfer from Pt of the surface to N embedded in C matrix as a consequence of Pt-N site formation and/or strong interaction between PtCo alloy and Pt/Co-N-C substrate. The Co XPS result shows a re-distribution from Co^0 dominated surface to more Co-N_x terminations after NH_3 treatment (Figure 2B), indicating the formation of the additional PGM-free active sites. Analysis of the N 1s XPS spectrum from PtCo@Pt-Co-GNF-BN reveals three groups of N functionalization (Figure 2C): pyridinic- (398.6 eV), pyrrolic- (400.2 eV), and oxidic-N (402–405 eV).[33] NH_3 treatment leads to additional N incorporated into the C matrix, and decomposition of pyrrolic N to form additional pyridinic groups.[27,34] As a consequence, the surface is dominated with pyridinic N (Figure 2C). This surface modification by creating additional Co-N_x and pyridinic N, would positively influence the electrocatalytic activity and electronic conductivity of the catalyst.[4,29,33]

X-ray absorption near-edge structure (XANES) at the Co K edge in PtCo@Pt-Co-GNF-BN includes contributions from metallic Co and Co-N_x with four different

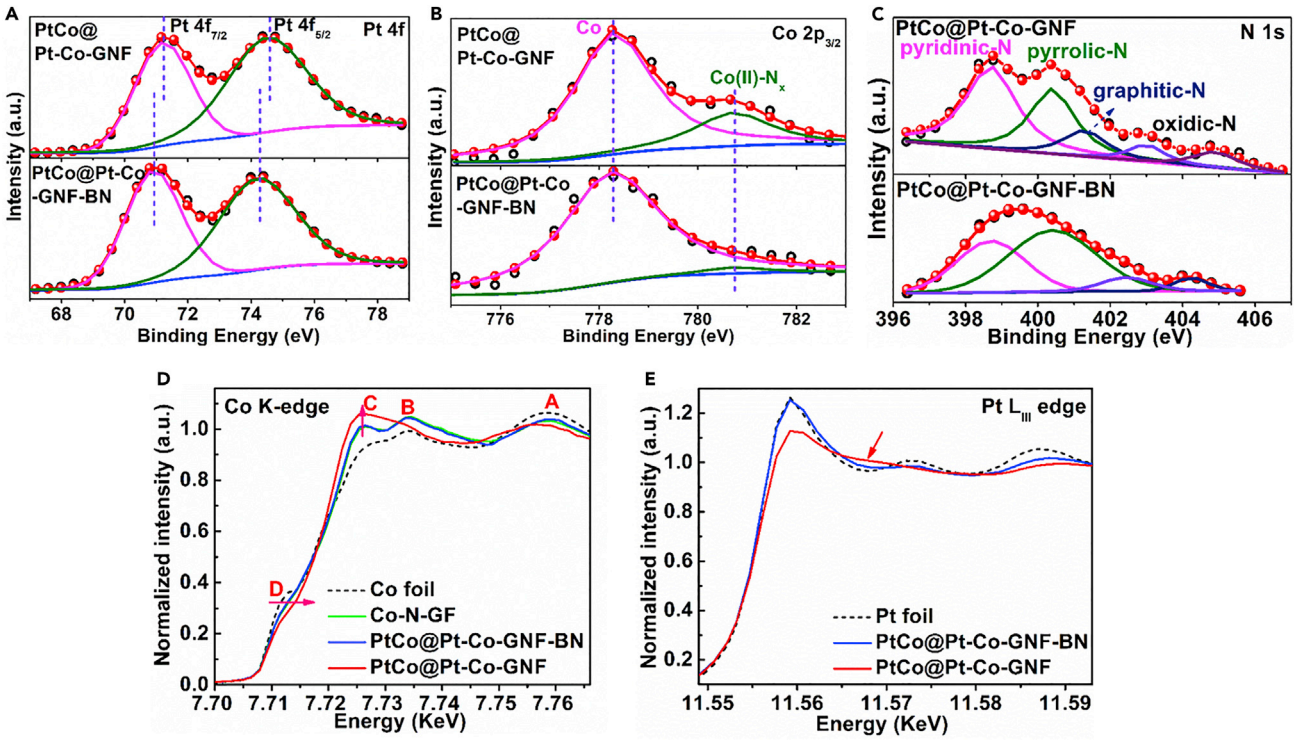

Figure 2. Structural characterization of the PtCo@Pt-Co-GNF catalyst

(A–C) XPS spectra of (A) Pt 4f, (B) Co $2p_{3/2}$, and (C) N 1s binding energy before (-BN) and after NH_3 treatment.

(D and E) *Ex situ* XANES spectra at (D) Co K edge and (E) Pt L_{III} edge before and after NH_3 treatment with the metal foil as reference.

features, labeled as A, B, C, and D (Figure 2D). After NH_3 treatment, features A and B were shifted to lower energy, suggesting the formation of Co–Pt bonds.[35] Feature D was blue shifted, suggesting that Co was positively charged. The intensity of feature C increased substantially, reflecting hybridization of Co 4s and 4p orbitals by Pt in the alloy[35] and N in Co-N_x. The extended X-ray absorption fine structure (EXAFS) displayed enhanced peak intensity at 1.44 Å after NH_3 treatment associated with Co-N/C contributions (Figures S10A and S10B). EXAFS fitting determined that the Co ion was coordinated by four N atoms at 1.93 Å in PtCo@Pt-Co-GNF (Figure S11, Table S2).[30,36,37] Besides Co–N scattering, Co K-edge EXAFS fitting reflected a mixture of contributions from Co–Co at 2.53 Å and Co–Pt at 2.65 Å. The XANES spectrum at Pt L_{III} edge in PtCo@Pt-Co-GNF suggested the formation of PtCo alloy as shown by the appearance of a peak at 11,576 eV[35,38] (Figure 2E, red arrow). The white line (WL) intensity at Pt L_{III} edge in PtCo@Pt-Co-GNF decreased relative to that in PtCo@Pt-Co-GNF-BN, indicating electron transfer from Co to Pt in the bulk material, which tuned the Pt d-band energy leading to weakened OH_{ad} binding on the Pt surface, and thus high catalytic activity toward ORR.[4] The formation of PtCo alloy was further confirmed by EXAFS (Figures S10C and S12). It is worth noting that $R_{Pt\text{-}Co}$ (2.19 Å) is similar to the $R_{Co\text{-}Co}$ (2.18 Å), suggesting that the majority of the hetero-atomic interactions in PtCo@Pt-Co-GNF are located in the Co-rich core, consistent with the $Pt_{thin\text{-}shell}$/single-$PtCo_{core}$ structure as shown in the atomic-resolution Z-contrast HAADF-STEM image (Figure 1E).

Electrocatalytic performance evaluation

A series of optimizations on the basis of activity evaluation in a single PEM cell achieved the best-performing PtCo@Pt-Co-GNF cathodic catalyst

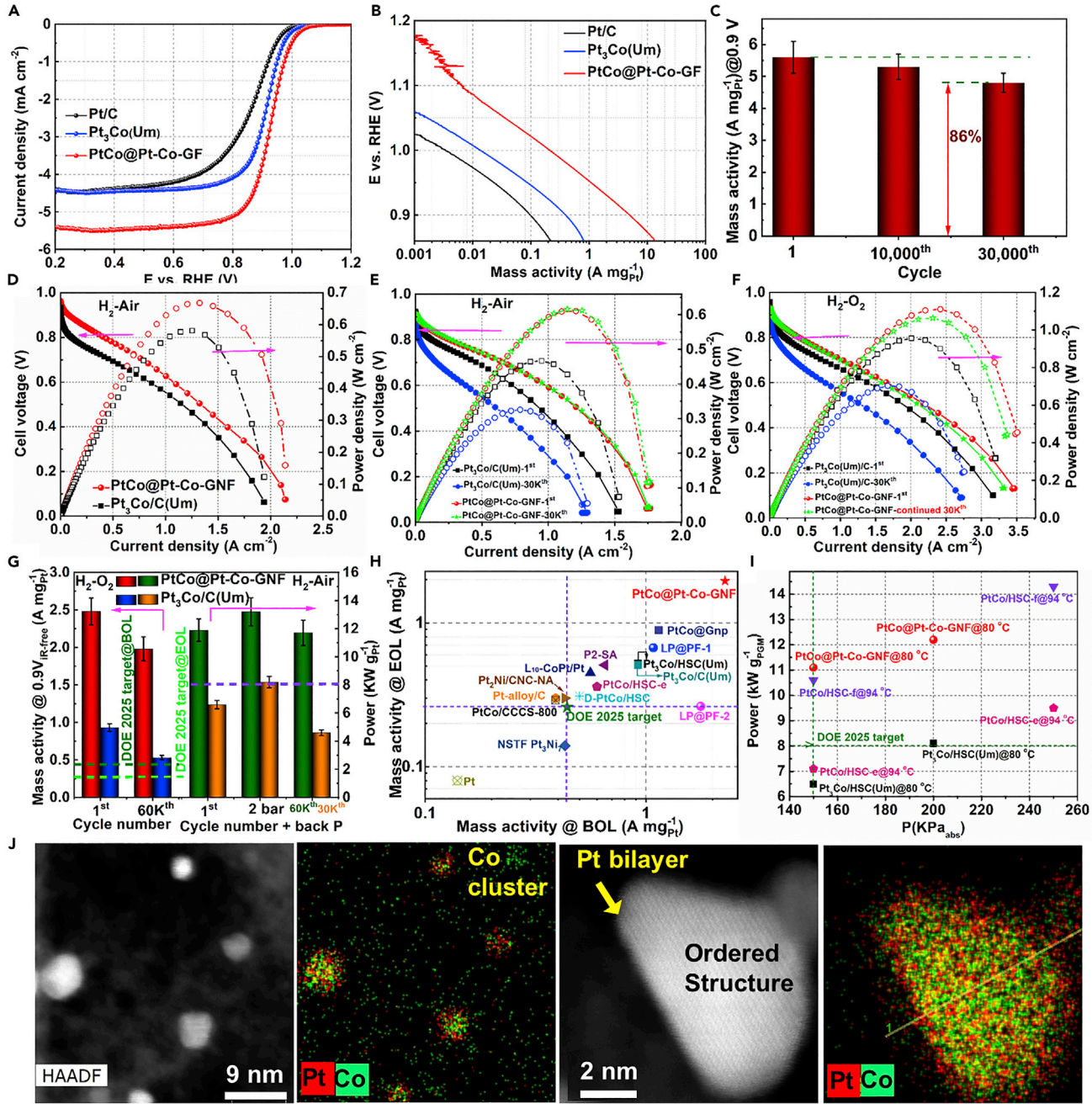

Figure 3. Electrochemical performance evaluation of PtCo@Pt-Co-GNF

(A) Steady-state ORR polarization plot of PtCo@Pt-Co-GNF recorded at a scan rate of 10 mV s^{-1} and 1,600 rpm in O_2-saturated 0.1 M $HClO_4$ electrolyte and compared with that of 20 wt % Pt/C and 30 wt % Pt_3Co/C(Um).

(B) The corresponding MA Tafel plots.

(C) Pt MA at 0.9 V of PtCo@Pt-Co-GNF as function of cycle number by RRDE.

(D) H_2-air fuel cell polarization and power density plots of PtCo@Pt-Co-GNF under Pa=Pc = 200 kPa_{abs}. MEA with 30 wt % Pt_3Co/C(Um) as cathodic catalyst was tested under the same conditions as benchmark.

(E) H_2-air fuel cell current-voltage (I-V) polarization and power density before and after 30,000 AST cycles under Pa=Pc = 150 kPa_{abs}.

(F) H_2-O_2 fuel cell i-v polarization and power density at initial step (before AST in H_2-air cell) and after 30,000 cycles of AST in H_2-O_2 cell (60,000 cycles in total, including the first 30,000 cycles in H_2-air cell and the continued second 30,000 cycles in H_2-O_2 cell) under Pa=Pc = 150 kPa_{abs}. H_2-air and H_2-O_2 fuel cell performance tests were conducted on the same MEA; that is 60,000 AST cycles in total for MEA with PtCo@Pt-Co-GNF as cathodic catalyst.

Figure 3. *Continued*

(G) Fuel cell MA at 0.9 $V_{iR\text{-}free}$ and power per gram of Pt before and after 30,000 AST in H_2-air cell and the continued 30,000 AST in H_2-O_2 cell.

(H) MAs of different catalysts at 0.9 $V_{iR\text{-}free}$ before and after 30,000 AST in PEMFC. Catalysts include those from this work and previous reported ones: LP@PF-1/2,[4] L_{10}-CoPt/Pt,[39] P_2-SA,[40] NSTF Pt_3Ni_7,[41] Pt_2Ni/CNC-NA,[42] PtCo/HSC-e,[43] Pt-alloy/C and Pt,[3] PtCo/CCCS-800,[44] and PtCo@Gnp.[45]

(I) Power per gram PGM of catalysts from this work and previous reports.[43]

(J) HAADF-STEM image of PtCo alloy NPs in PtCo@Pt-Co-GNF after 60,000 AST cycles; the corresponding EDS elemental mapping, Pt versus Co; atomic-resolution Z-contrast HAADF-STEM image of a representative PtCo alloy NP after AST; the corresponding Pt versus Co elemental mapping. For all the fuel cell tests, membrane = Nafion 211, temperature = 80°C, cathode loading $\leq$0.048 mg_{Pt} cm^{-2}, anode loading $\leq$0.035 mg_{Pt} cm^{-2} (Pt loading was determined by ICP-MS and X-ray fluorescence (XRF) methods, Figure S40); $RH_a = RH_c = 100\%$. For H_2-air cell, $P_{H2} = P_{Air}$ = 150 kPa_{abs} or 200 kPa_{abs}; H_2 flow rate = 200 mL min^{-1} (2.8 stoichiometry at 2.0 A cm^{-2}), and air flow rate = 780 mL min^{-1} (4.6 stoichiometry at 2.0 A cm^{-2}, 3.5 kPa pressure drop at 2.0 A cm^{-2}); for H_2-O_2 cell, $P_{H2} = P_{O2}$ = 150 kPa_{abs}, H_2 flow rate = O_2 flow rate = 200 mL min^{-1}.

(Figures S13–S16; Tables S3 and S4). The Pt/C and the state-of-the-art Pt_3Co/C catalyst from Umicore, Pt_3Co/C(Um), as well as Co-N-GF were tested under the same conditions as benchmarks and control sample, respectively. RRDE testing in O_2-saturated 0.1 M $HClO_4$ revealed a half-wave potential of 0.93 V (versus reversible hydrogen electrode, RHE) for PtCo@Pt-Co-GNF, ~170 mV higher than that of Co-N-GF (~0.76 V) (Figure 3A, Figure S17A). The average number of transferred electrons per O_2 molecule (ne) was 3.94–3.99, corresponding to a low H_2O_2 yield of <3% (Figure S17C). By contrast, even with higher Pt loading than that in PtCo@Pt-Co-GNF, the half-wave potentials of Pt/C and Pt_3Co/C(Um) were 0.86 and 0.91 V, respectively, which were 70 and 20 mV lower than that of PtCo@Pt-Co-GNF. Tafel plots of mass activities (MAs) obtained from Figure 3A normalized by the total mass of the loaded Pt exhibited a slope of 63 mV dec^{-1} for PtCo@Pt-Co-GNF (Figure 3B), significantly lower than that of Pt/C (89 mV dec^{-1}) and Pt_3Co/C(Um) (71 mV dec^{-1}), suggesting the better ORR kinetics of the former. Furthermore, the PtCo@Pt-Co-GNF displayed an MA of 5.48 $\pm$ 0.41 A mg_{Pt}^{-1} at 0.9 V, ~56 and ~14 times higher than that of Pt/C (0.098 $\pm$ 0.003 A mg_{Pt}^{-1}) and Pt_3Co/C(Um) (0.39 $\pm$ 0.03 A mg_{Pt}^{-1}), respectively. The Pt MA loss after 30,000 potential cycles by means of RRDE was 14% (Figures 3C and S18). To check the structure stability, we performed inductively coupled plasma mass spectroscopy (ICP-MS) to assess whether any metal had leached into the electrolyte. We detected 0.3 wt % Co and 0.02 wt % Pt being shed into the electrolyte, corroborating the excellent durability under acid.

The high ORR activity measured through RRDE does not directly reflect the performance in a practical fuel cell due to the fundamentally different operating conditions (e.g., temperature, electrolyte, electrode structure). To measure its fuel cell performance, we integrated PtCo@Pt-Co-GNF into an MEA, evaluated its performance in an operating PEMFC including H_2-air and H_2-O_2 cells, and benchmarked to Pt_3Co/C(Um). For comparison, the Pt loadings at cathode and anode for all the MEAs were $\leq$0.048 mg_{Pt} cm^{-2} and $\leq$0.035 mg_{Pt} cm^{-2}, respectively. For each test, MEA was manufactured and tested for reproducibility purposes for at least three times. A series of optimizations regarding water management achieved high energy efficiency and high power density for PtCo@Pt-Co-GNF in fuel cells (Figures S19 and S20). It is worth noting that the catalytic activity of Co-N-GF for ORR in PEMFCs can be compared with other MEAs reported in the literature for PGM-free catalysts under realistic PEMFC operation conditions (Figure S21).[16,46,47] After integration with 4.8 $\pm$ 0.2 wt % Pt, the PtCo@Pt-Co-GNF demonstrated an unprecedented ORR activity and sustained durability in an operating PEM fuel cell, as discussed below. Figure 3D shows H_2-air cell performance at 200 KPa_{abs}. The current-voltage polarization profile of PtCo@Pt-Co-GNF was dramatically higher than that of Pt_3Co/C(Um) throughout the polarization curve. In addition, the current density at 0.8 V was 438 mA cm^{-2} for PtCo@Pt-Co-GNF, four times higher than that of Pt_3Co/C(Um) (106 mA cm^{-2} at 0.8 V). In the mass transport region at 1.75 A cm^{-2} current density, a

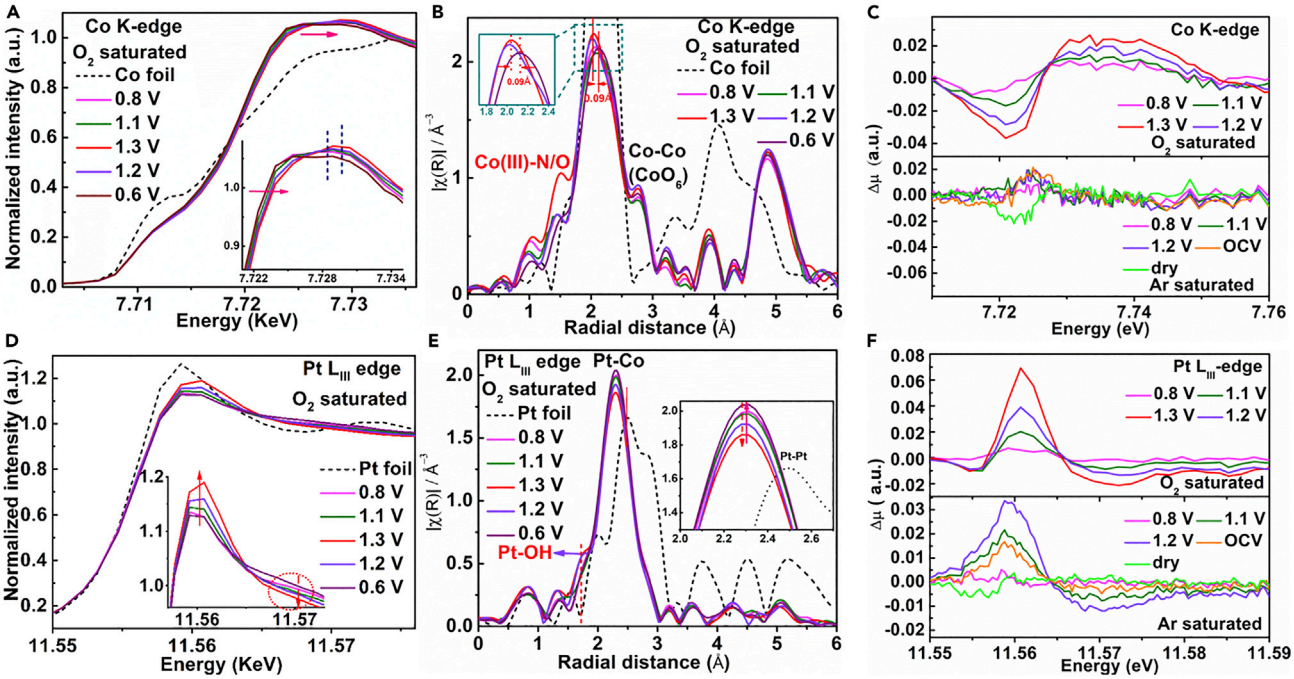

Figure 4. *In situ* X-ray absorption spectra of PtCo@Pt-Co-GNF

(A) Co K-edge XANES spectra measured at different potentials ascending from 0.8 V, 1.1 V, to 1.3 V and then descending to 1.2 V and 0.6 V in O_2-saturated 0.1 M $HClO_4$ electrolyte. Insets magnify the WL region, showing structure evolution during the ORR process.

(B) Fourier transform (FT) EXAFS spectra at Co K edge collected at potentials ascending from 0.8 V, 1.1 V, to 1.3 V and then descending to 1.2 V and 0.6 V in O_2-saturated 0.1 M $HClO_4$ electrolyte. Insets are enlargements of Co–Co peaks.

(C) Differential Δμ (Δμ(E)-Δμ(0.6 V)) XANES spectra at Co K edge in O_2- (top) and Ar- (bottom) saturated 0.1 M $HClO_4$ recorded at the indicated potentials at room temperature.

(D) Pt L_{III}-edge XANES spectra measured at different potentials ascending from 0.8 V, 1.1 V, to 1.3 V and then descending to 1.2 V and 0.6 V in O_2-saturated 0.1 M $HClO_4$ electrolyte. Insets magnify the WL region, showing local atomic environment changes during the ORR process.

(E) FT EXAFS spectra at Pt L_{III} edge collected at potentials ascending from 0.8 V, 1.1 V, to 1.3 V and then descending to 1.2 V and 0.6 V in O_2-saturated 0.1 M $HClO_4$ electrolyte. Insets are enlargements of Pt-Co peaks.

(F) Differential Δμ (Δμ(E)-Δμ(0.6 V)) XANES spectra at Pt L_{III} edge in O_2- (top) and Ar- (bottom) saturated 0.1 M $HClO_4$ recorded at the indicated potentials at room temperature.

significant reduction in voltage loss of up to 136 mV was achieved in PtCo@Pt-Co-GNF relative to Pt_3Co/C(Um).

We performed AST to investigate the durability of PtCo@Pt-Co-GNF in H_2-air cell followed by H_2-O_2 cell on the same MEA for a total of 60,000 voltage cycles, following the US Department of Energy (DOE) durability evaluation protocol for ORR catalysts in PEMFCs.[5] At 150 kPa_{abs} pressure in the H_2-air cell (Figure 3E), the initial performance of PtCo@Pt-Co-GNF was superior to that of Pt_3Co/C(Um) in terms of limiting current density and peak power density (1.75 A cm^{-2} and 0.63 W cm^{-2} versus 1.5 A cm^{-2} and 0.45 W cm^{-2}) throughout the voltage range. After 30,000 AST cycles, the voltage loss at 0.8 A cm^{-2} was negligible for PtCo@Pt-Co-GNF, surpassing the target set by DOE (<30 mV loss at 0.8 A cm^{-2} after 30,000 AST cycles).[5] The peak power density was also maintained, indicating that the catalyst is extremely durable for PEMFCs. By contrast, the voltage loss at 0.8 A cm^{-2} for Pt_3Co/C(Um) was 156 mV, and the peak power density showed 31% decay after 30,000 AST cycles (Figure 3E). Power per gram of PGM (kW g_{PGM}^{-1}) is a valuable metric for the evaluation of PGM catalyst being used in vehicles. Compared with DOE's 2025 target of 8 kW g_{PGM}^{-1}, the Pt power metric of PtCo@Pt-Co-GNF at

both the beginning of life (BOL; 11.9 ± 0.8 kW g_{Pt}^{-1} at 150 kPa_{abs}, 13.2 ± 1.0 kW g_{Pt}^{-1} at 200 kPa_{abs}) and end of life (EOL; 11.7 ± 0.9 kW g_{Pt}^{-1} at 150 kPa_{abs}) after 30,000 test cycles in an H_2-air cell are noteworthy (98% retention, Figure 3G, right). In contrast, Pt_3Co/C(Um) failed to meet DOE's target at BOL and ended up with serious decay at EOL.

The MEA with PtCo@Pt-Co-GNF as cathodic catalyst after 30,000 AST cycles in an H_2-air cell was further subjected to 30,000 AST cycles in an H_2-O_2 cell. Figure 3F shows the initial polarization curves of PtCo@Pt-Co-GNF in an H_2-O_2 cell before AST and at EOL (after 60,000 AST cycles) and benchmarked to Pt_3Co/C(Um). Because Pt_3Co/C(Um) was seriously deactivated after durability measurement in the H_2-air cell, we prepared a new MEA with Pt_3Co/C(Um) at the cathode. Even having undergone 30,000 AST cycles in the H_2-air cell, the H_2-O_2 cell performance with PtCo@Pt-Co-GNF at the cathode still outperformed the fresh Pt_3Co/C(Um) and PtCo/XC-72 (Figure S22), respectively, displaying higher limiting current density and peak power density throughout the voltage range (Figure 3F, iR-corrected polarization shown in Figure S23). This result corroborates the pivotal role of Pt-Co-GNF substrate on the overall ORR activity and durability of the catalyst. The peak power density of PtCo@Pt-Co-GNF reached 1.11 W cm^{-2} at BOL (150 kPa_{abs}), corresponding to an effective Pt utilization of 0.041 ± 0.003 g_{Pt} kW^{-1} at cathode. The PtCo@Pt-Co-GNF delivered an MA of 2.48 ± 0.18 A g_{Pt}^{-1} at 0.9 $V_{iR\text{-}free}$ at BOL (Figure 3G, left), 2.7 times that of Pt_3Co/C(Um) (0.92 A g_{Pt}^{-1} at 0.9 $V_{iR\text{-}free}$), and 5.6 times the DOE's 2025 target of 0.44 A g_{Pt}^{-1} at 0.9 $V_{iR\text{-}free}$. After the 60,000 AST cycles, including 30,000 cycles in H_2-air cell followed by 30,000 cycles in H_2-O_2 cell, the MA of PtCo@Pt-Co-GNF maintained 80% retention (1.98 ± 0.16 A g_{Pt}^{-1} at 0.9 $V_{iR\text{-}free}$ at EOL) (Figure 3G, left), exceeding the DOE's target, which requires less than 40% loss of initial MA after the 30,000-cycle AST (0.26 A g_{Pt}^{-1} at EOL). In comparison, Pt_3Co/C(Um) displayed obvious degradation with MA loss of 45% (0.51 A g_{Pt}^{-1} at 0.9 $V_{iR\text{-}free}$ after only 30,000 cycles). Moreover, we note that the PtCo@Pt-Co-GNF EOL MA (1.98 ± 0.16 A mg_{Pt}^{-1}) is 7.6 times that of the DOE target (0.264 A mg_{Pt}^{-1}) and four times that of Pt_3Co/C(Um) (0.51 A mg_{Pt}^{-1}), respectively. To the best of our knowledge, the MAs of PtCo@Pt-Co-GNF at BOL and EOL rank among the highest for PGM catalysts reported in PEMFCs so far (Figures 3H and 3I; Table S5).[3,4,39–45] In addition, a chronopotentiometry measurement in PEMFC at constant voltage of 0.7 V producing 1.0 A cm^{-2} current density lasted for 100 h without degradation (Figure S24). Our results suggest that PtCo@Pt-Co-GNF is a potential promising candidate for widespread fuel cell application in autos.

Possible mechanism during ORR

The morphology of the interconnected C nanofiber with MOF-structured beads in PtCo@Pt-Co-GNF was maintained after the 60,000 AST cycles in fuel cell and EDS, which attested to the negligible changes in atomic ratios of Co:Pt:N:C (Figure S25). The average particle size and the core-shell-structured PtCo alloy with mono-/bilayer Pt shell were also preserved (Figures 3J and S26). All these results suggest the durable structure of PtCo@Pt-Co-GNF under the harsh operating conditions of PEMFC. To better understand the origin of this extraordinary ORR performance, we collected *operando* XANES and EXAFS spectra at the Co K edge and Pt L_{III} edge in O_2- and Ar-saturated 0.1 M $HClO_4$, respectively, at various applied potentials to examine the evolution of local atomic structure and/or metal oxidation states for PtCo@Pt-Co-GNF proceeding ORR (Figures 4, S27 and S28). For comparison, we also performed the *operando* XANES and EXAFS on Pt_3Co/C(Um) in Ar-saturated 0.1 M $HClO_4$ electrolyte at three representative potentials (0.42 V, 0.8 V, and

1.1 V; Figure S29). When 0.8 V potential was applied on PtCo@Pt-Co-GNF in O_2-saturated 0.1 M $HClO_4$, XANES spectrum at Co K edge showed that the absorption energy was slightly blue shifted compared with the dry sample (Figure S30A), suggesting the absorption of oxygenated species (O* or OH*) on the surface of Co. This phenomenon is similar to a previous report presented by Frédéric Jaouen's group on $Co_{0.5}$-N-C catalyst in O_2-saturated 0.1 M $HClO_4$ where oxygenated species were absorbed onto Co active sites at both 0.2 V and 0.8 V.[30] Co K-edge XANES spectra were slightly shifted to higher energy as a function of ascending potential (Figure 4A, inset). As the applied potential increased to 1.3 V, the absorption edge at 7,728 eV shifted to 7,729 eV with slightly enhanced WL intensity, indicating charge transfer from Co to the oxygenate intermediate. The variation was clearly discerned from the surface sensitive $\Delta\mu$-XANES profile (Figure 4C, top). The amplitude of $\Delta\mu$ increased with increasing the applied potential, indicating that the Co(II)-N_4 sites were progressively occupied by OH_{ads} at elevated potential, similar to what occurred on Fe^{2+}-N_4 sites during ORR.[48] EXAFS spectrum at Co K edge at 0.8 V (Figures 4B and S30B) displayed the appearance of Co–Co bonds at 2.78 Å, which showed that Co atoms were interconnected by di-μ-xox (μ_3-O)(μ_2-OH) bridges forming an edge-sharing Co octahedron.[49] The new peak at 4.86 Å further confirmed the edge-sharing CoO_6 octahedron structure. The Co-deficient CoO_6 structure, along with the di-μ-xox bridge was observed during catalytic reaction for the active Co-Cat.[50] Different from $Co_{0.5}$-N-C in the ORR region where no obvious change was detected,[30] Co-N_4 of PtCo@Pt-Co-GNF showed drastic changes in terms of oxidation state and local atomic structure with electrochemical potential, revealing an enhanced catalytic activity of Co moieties, which may be ascribed to the synergy of Pt sites. At 1.2 and 1.3 V, the Co–Co bond distance decreased by 0.09 Å relative to that at 0.8 V (Figure 4B, inset). Moreover, a new peak at 1.49 Å appeared at 1.3 V, which might be associated with Co(III)N_x moieties formed after the transition of Co(II)/Co(III) at $\sim$ 1.25 V (Figure S27B), similar to that observed in $Co_{0.5}$-N-C catalyst at 1.3 V.[30] However, the change for Co-N_4 sites in the ORR region in Ar-saturated electrolyte was virtually unnoticeable (Figure 4C, bottom; Figure S28A). This result suggests that the adsorption of O_2/oxygen intermediates on Co-N_4 moieties takes place only in O_2-saturated electrolyte, with the Co–O bond originating from O_2.

WL intensity at Pt L_{III} edge increased at elevated potential in O_2-saturated electrolyte (red arrow, Figure 4D), accompanied with intensity decrease in the post-edge region (red circle). This result indicates the absorption of oxygenated intermediate on the Pt surface, which increases the unoccupied d-orbitals of Pt via the charge transfer from Pt to O.[51] It is worth noting that the WL intensity at 1.3 V is still lower than that of Pt foil, emphasizing the metallic state of Pt. EXAFS spectra at Pt L_{III} edge showed decreased Pt-Co peak intensity with increasing potential (Figure 4E, inset), suggesting that the surface became disordered during ORR. Indeed, the Debye-Waller factor σ^2 increased as function of ascending potential, further verifying the increased disorder degree of the Pt surface at high potential during ORR (Figure S31; Table S6). As the potential reached 1.3 V, a new weak peak at 1.72 Å appeared (Figure 4E). This peak is assigned to a Pt–OH bond, which is 0.12 Å larger than the Pt–O bond (1.6 Å).[51,52] *Operando* XANES and EXAFS spectra collected at Pt L_{III} edge in Ar-saturated electrolyte showed the same trend as that observed in O_2-saturated electrolyte (Figure S28B). This result supports the fact that O_2 or oxygen intermediates adsorption on Pt is much stronger than that on Co-N_4 moieties. The variation on Pt sites as a function of applied potential in Ar-saturated electrolyte similar to that in O_2-saturated electrolyte is magnified in the experimental $\Delta\mu$ (Figure 4F). We did not observe energy shift at any applied

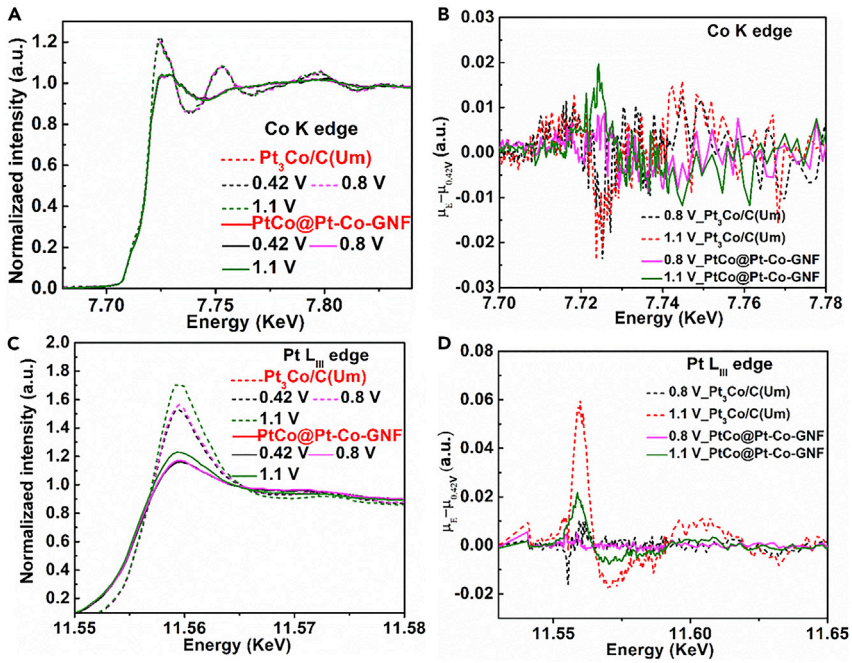

Figure 5. *In situ* X-ray absorption spectra of PtCo@Pt-Co-GNF in Ar-saturated 0.1 M $HClO_4$ electrolyte

(A) XANES spectra at Co K edge recorded at representative potentials of 0.42 V, 0.8 V, and 1.1 V in Ar-saturated 0.1 M $HClO_4$ electrolyte for sample PtCo@Pt-Co-GNF and compared with that for $Pt_3Co/C(Um)$.

(B) Differential Δμ XANES spectra at Co K edge for sample PtCo@Pt-Co-GNF and compared with that for $Pt_3Co/C(Um)$.

(C) XANES spectra at Pt L_{III} edge recorded at representative potentials of 0.42 V, 0.8 V, and 1.1 V in Ar-saturated 0.1 M $HClO_4$ electrolyte for sample PtCo@Pt-Co-GNF and compared with that for $Pt_3Co/C(Um)$.

(D) Differential Δμ XANES spectra at Pt L_{III} edge for sample PtCo@Pt-Co-GNF and compared with that for $Pt_3Co/C(Um)$.

potential in either O_2-saturated or Ar-saturated electrolyte in the Pt Δμ spectra, suggesting no O_2 penetration through the Pt shell to the subsurface to bind to Co, as the oxidation of subsurface Co in the PtCo core would cause energy blue shift in Δμ spectra.[53] This result shows that the Co in the PtCo core is well protected by the Pt shell against being oxidized during ORR. Furthermore, this result indirectly suggests that the variation of Co in O_2-saturated electrolyte shown in Δμ spectra may exclusively be associated with Co-N_4 moieties. When the potential decreased to 0.6 V, both XANES and EXAFS spectra at Co K edge and Pt L_{III} edge reverted to their initial state, which indicated that the chemical absorption of oxygenate intermediates on Co moieties and Pt sites was a reversible process during ORR. The Δμ spectrum of PtCo@Pt-Co-GNF dry sample at Co K edge suggested a weak O_2 adsorbate coverage (coming from the air) over the exposed Co moieties (Figure 4C, bottom), whereas at Pt L_{III} edge indicated a clean surface (Figure 4F, bottom). XANES, EXAFS, and Δμ spectra of PtCo@Pt-Co-GNF at open circuit voltage (OCV = ~ 0.96 V) resemble those of electrodes at potential of 1.1 V for both Co and Pt. Compared with that of $Pt_3Co/C(Um)$ catalyst, the WL intensity at Co K edge and Pt L_{III} edge of PtCo@Pt-Co-GNF are low during ORR (Figures 5A and 5C), indicating low electron vacancies in the 4p orbitals of Co atoms and 5d orbitals of Pt atoms; namely, low oxidation states of Co and Pt, respectively. High oxidation state of Pt is prone to leach to the acid. In addition, the magnitude

of the change on Pt sites for PtCo@Pt-Co-GNF is less significant in Δμ spectra than that for Pt_3Co/C(Um) (Figure 5D), implying a weakened binding energy of O_2/oxygen intermediate to Pt in PtCo@Pt-Co-GNF relative to that in Pt_3Co/C(Um), which may be ascribed to the synergy effect between Pt and Co moieties, resulting in a higher ORR activity of PtCo alloy in PtCo@Pt-Co-GNF. The *operando* experiments unequivocally reveal a synergistic effect between Pt sites and Co-N_4 sites optimizing both Co and Pt electronic configurations toward improved catalytic activities, respectively, for ORR. Meanwhile, it discloses that both PtCo NP and Pt-Co-GNF simultaneously contribute to the ORR activity. In addition, the Δμ spectra at Co K edge showed the negative peak contribution around 7.72 keV in the Pt_3Co/C(um), revealing the formation of subsurface O in the Pt_3Co NPs during ORR process,[53] which implies the subsurface Co atoms were oxidized. In contrast, we did not observe the subsurface O in the PtCo NPs of PtCo@Pt-Co-GNF from Δμ spectra either at Co K edge or Pt L_{III} edge, suggesting good protection of the PtCo core by the Pt shell during ORR. Compared with the Pt_3Co/C(Um), the lower H_2O_2 formation (Figure S17C), the stronger affinity of PtCo NPs to the substrate (indicated by the theory calculation shown as below), along with the well-protected PtCo NP due to the core-shell structure are responsible for the exceptional durability in PEMFC operation.

We performed DFT simulation for deciphering the reaction mechanism behind the significantly enhanced performance of PtCo@Pt-Co-GNF toward ORR. Considering that the structure of the PtCo@Pt-Co-GNF consisted of PtCo NPs and Pt-Co-N_5 graphene fiber, the ORR pathways at U = 0.9 V versus RHE on Co-N_4 moieties (with curvature) and Pt sites of PtCo NPs were simulated, mimicking a condition under fuel cell operation. The same simulation on Co-N_4 in planar graphene matrix was also included for comparison. Four elementary reaction steps, including the generation of OOH* from the absorbed O_2, and further reduction to O* and OH* were included for the mechanism simulation.[54,55] Over the Co-N_4 sites, the reaction can either proceed with the four-electron pathway to produce H_2O or the two-electron pathway to generate H_2O_2. It is worth noting that the former is more favorable than Co-N_4 with curvature configuration. For example, compared with the Co-N_4 in the planar graphene matrix, the Co-N_4 with curvature lowers the reaction thermodynamic barrier for the $4e^-$ to proceed (Figure 6A, purple dot line versus red solid line; Figures S32 and S33), making the reaction toward H_2O more achievable than H_2O_2 at 0.9 V, and thus suppressing the formation of H_2O_2 indirectly. Our calculation shows that the curvature effect to the Pt site is negligible due to the high catalytic activity of Pt. However, Pt decomposes H_2O_2 produced by the Co-N_4 site, as H_2O_2 releases freely from the Co-N_4 site and migrates to the nearby Pt, in line with the result obtained from RRDE, where the H_2O_2 yield is the lowest in PtCo@Pt-Co-GNF (Figure S17C). Therefore, the suppression/mitigation of H_2O_2 formation by the enhanced curvature and Pt sites mitigates the demetallation of the Co-N_4 sites and the C oxidation, leading to a less corrosive environment for Co-N_4 moieties and C substrate and, thereby, exceptional catalytic durability for ORR. In addition, our calculation suggests a stronger interaction between PtCo and G-Pt/Co-N_5 substrate than between PtCo and pure graphene (Figures 6C and 6D; Table S8). Those results, along with the high C graphitization, should be responsible for the significantly improved stability, enabling PtCo@Pt-Co-GNF sustained for 60,000 AST cycles in PEMFCs with negligible changes in structure and composition. The schematic diagram of reactions on the surface of PtCo@Pt-Co-GNF is outlined in Figure 6B. We also studied the effect of single Pt on the catalytic activity of Co-N_4, revealing a significantly enhanced ORR activity of Co-N_4 in the Pt-Co-N_5 configuration, which

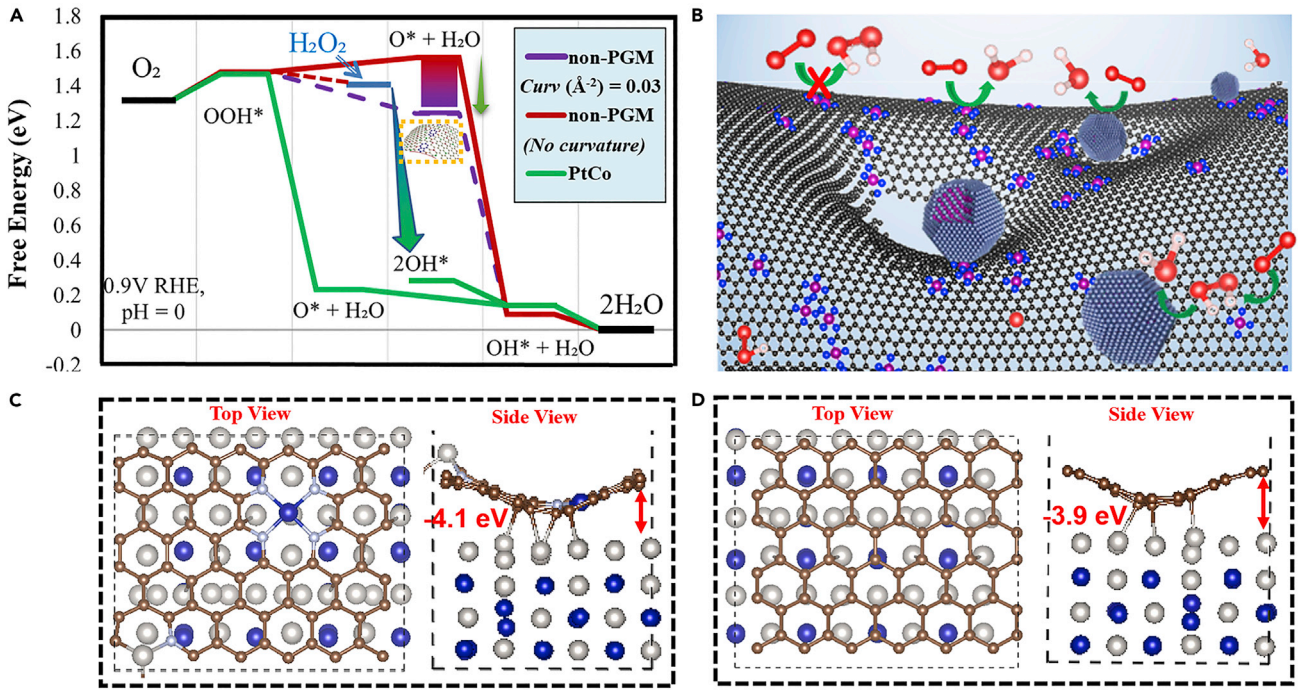

Figure 6. DFT study of the ORR mechanism and stability of PtCo@Pt-Co-GNF

(A) Free-energy diagrams of the ORR pathways: red and purple denote the ORR pathway on the Co-N_4 embedded in graphene, with red representing the planar structure and purple highlighting how the pathway is modified with changes to the local curvature; small arrow denotes that the thermodynamic barrier is decreased significantly on Co-N_4 in the curved local structure compared with that in the planar structure; blue denotes H_2O_2 generated over Co-N_4 sites; big arrow denotes H_2O_2 migrating to the strained Pt (111) sites and being broken down by Pt; green denotes the ORR pathway on the strained Pt.

(B) Schematic diagram of reactions on the surface of PtCo@Pt-Co-GNF catalyst.

(C) Top view and side view of the interfacial distance between PtCo NP and G-Pt/Co-N_5.

(D) Top view and side view of the interfacial distance between PtCo NP and G.

may be one of the factors contributing to the significantly improved catalytic activity of PtCo@Pt-Co-GNF (Figures S34–S39). Therefore, all single-atom Pt, Co-N_4 sites, and PtCo NPs, as well as graphene, are both essential and indispensable to the high catalytic activity and sustained durability.

Conclusions

We have presented a facile and robust method for preparation of highly durable and active PtCo@Pt-Co-GNF catalyst composed of core-shell-structured PtCo NP dispersed on the ORR self-active Pt-Co-GNF fibrous substrate. Benefiting from the combination of Co-ZIF and PAN fiber in the precursor, along with the *in situ* reduction of Pt cluster by using the solvothermal method, the Pt-Co-GNF substrate possesses (1) densely populated Co-N_4 active sites and a trace amount of atomic Pt, (2) tailored high porosity and high surface area, (3) interconnected micro-/macro-pores, and (4) N-doped graphene fiber. Such a unique structure endows the substrate relatively high catalytic activity toward ORR. Therefore, after integration with ultra-low loading of Pt, MEA assembled with PtCo@Pt-Co-GNF as cathodic catalyst at demanding Pt loading (anode + cathode of $\leq 0.083\ mg_{Pt}\ cm^{-2}$) delivered an unprecedented Pt MA of $2.48 \pm 0.18\ A\ g_{Pt}^{-1}$ at $0.9\ V_{iR\text{-}free}$, $438\ mA\ cm^{-2}$ current density at 0.8 V in H_2-air cell, and an exceptional durability with 80% MA retention after 60,000 AST cycles, surpassing the DOE's 2025 target for ORR catalysts under PEMFC conditions. The MEA displayed an effective Pt utilization of 0.041 ±

0.003 g_{Pt} kW^{-1} in H_2-O_2 cell, and 11.9 $\pm$ 0.8 kW g_{PGM}^{-1} at 150 kPa_{abs} in H_2-air cell. These performance metrics enable a fuel-cell-powered vehicle to be competitive with ICE autos. Insights obtained from the *operando* XANES and EXAFS experiments revealed that modifying the C matrix with single Pt strengthened the binding energy of oxygen intermediates at Co moieties, improving its ORR activity. *Operando* X-ray absorption response also revealed that, compared with that of commercial Pt_3Co/C(Um), the electronic configurations of Co and Pt were optimized toward high catalytic activity due to the synergistic effect between Co-N_4 and PtCo. Theoretical simulation revealed that the enhanced curvature of the substrate lowered the thermodynamic barriers for the $4e^-$ reaction to proceed over Co-N_4 sites, favoring the formation of H_2O and suppressing that of H_2O_2. The suppression of H_2O_2 formation by the curvature, the fast decomposition of H_2O_2 by Pt sites, the well protected PtCo NPs by the unique core-shell structure, and the strong affinity of PtCo to the Pt-Co-N substrate contribute to the exceptional durability of PtCo@Pt-Co-GNF under fuel cell operation. We believe that the unprecedented activity and sustained durability of PtCo@Pt-Co-GNF achieved through delicate morphology engineering would boost widespread commercialization of fuel cells in autos and beyond, which will help to reduce reliance on fossil fuels.

EXPERIMENTAL PROCEDURES

Resource availability

Lead contact

Further information and requests for resources and reagents should be directed to and will be fulfilled by the lead contact, Lina Chong (chonglina@sjtu.edu.cn).

Materials availability

This study did not generate any unique new reagents.

Data and code availability

All data are available in the main text or supplemental information.

SUPPLEMENTAL INFORMATION

Supplemental information can be found online at https://doi.org/10.1016/j.checat.2023.100541.

ACKNOWLEDGMENTS

We acknowledge use of Argonne National Laboratory's Advanced Photo Source, the DOE Office of Science User Facilities, supported by the DOE Office of Science, under contract DE-AC02-06CH11357. This work was performed, in part, at the Center for Nanoscale Materials, a US Department of Energy Office of Science User Facility, and supported by the US Department of Energy, Office of Science, under contract no. DE-AC02-06CH11357. Funding: this work was supported by regenerate fuel cell research under award number PRJ1006031 through the Maria Goeppert Mayer Fellowship at Argonne National Laboratory, Laboratory-Directed Research and Development office (LDRD), DOE, US. We acknowledge the support from US DOE Hydrogen and Fuel Cell Technologies office (HFTO).

AUTHOR CONTRIBUTIONS

L.C. designed research. L.C., H.Z., and Z.Y., performed the research. J.K., Q.T., and H.Z. performed DFT. J.G. conduced TEM. L.C., Z.H., Z.Y., and D.A. analyzed the data. L.C., I.B., D.A., J.K., J.Z., and W.D. wrote the paper. All the authors discussed and commented on the manuscript.

DECLARATION OF INTERESTS

The authors declare no competing interests.

Received: July 7, 2022
Revised: December 10, 2022
Accepted: February 6, 2023
Published: March 7, 2023

REFERENCES

1. Gasteiger, H.A., Kocha, S.S., Sompalli, B., and Wagner, F.T. (2005). Activity benchmarks and requirements for Pt, Pt-alloy, and non-Pt oxygen reduction catalysts for PEMFCs. Appl. Catal. B Environ. *56*, 9–35. https://doi.org/10.1016/j.apcatb.2004.06.021.

2. Wagner, F.T., Lakshmanan, B., and Mathias, M.F. (2010). Electrochemistry and the future of the automobile. J. Phys. Chem. Lett. *1*, 2204–2219. https://doi.org/10.1021/jz100553m.

3. Debe, M.K. (2012). Electrocatalyst approaches and challenges for automotive fuel cells. Nature *486*, 43–51. https://doi.org/10.1038/nature11115.

4. Chong, L., Wen, J., Kubal, J., Sen, F.G., Zou, J., Greeley, J., Chan, M., Barkholtz, H., Ding, W., and Liu, D.-J. (2018). Ultralow-loading platinum-cobalt fuel cell catalysts derived from imidazolate frameworks. Science *362*, 1276–1281. https://doi.org/10.1126/science.aau0630.

5. DOE FCTTR, US DRIVE Partnership (2017). Fuel Cell Technical Team Roadmap. https://www.energy.gov/sites/prod/files/2017/11/f46/FCTT_Roadmap_Nov_2017_FINAL.pdf.

6. Steele, B.C., and Heinzel, A. (2001). Materials for fuel-cell technologies. Nature *414*, 345–352. https://doi.org/10.1038/35104620.

7. Seh, Z.W., Kibsgaard, J., Dickens, C.F., Chorkendorff, I., Nørskov, J.K., and Jaramillo, T.F. (2017). Combining theory and experiment in electrocatalysis: insights into materials design. Science *355*, eaad4998. https://doi.org/10.1126/science.aad4998.

8. Shao, M., Chang, Q., Dodelet, J.-P., and Chenitz, R. (2016). Recent advances in electrocatalysts for oxygen reduction reaction. Chem. Rev. *116*, 3594–3657. https://doi.org/10.1021/acs.chemrev.5b00462.

9. R. Borup (2019). Fuel Cell Performance and Durability Consortium (US DOE). Annual Merit Review Proceedings. https://www.hydrogen.energy.gov/pdfs/review19/fc135_borup_2019_o.pdf.

10. Du, L., Prabhakaran, V., Xie, X., Park, S., Wang, Y., and Shao, Y. (2021). Low-PGM and PGM-free catalysts for proton exchange membrane fuel cells: stability challenges and material solutions. Adv. Mater. *33*, 1908232. https://doi.org/10.1002/adma.201908232.

11. Sheng, T., Tian, N., Zhou, Z.-Y., Lin, W.-F., and Sun, S.-G. (2017). Designing Pt-based electrocatalysts with high surface energy. ACS Energy Lett. *2*, 1892–1900. https://doi.org/10.1021/acsenergylett.7b00385.

12. Kongkanand, A., and Mathias, M.F. (2016). The priority and challenge of high-power performance of LowPlatinum proton-exchange membrane fuel cells. J. Phys. Chem. Lett. *7*, 1127–1137. https://doi.org/10.1021/acs.jpclett.6b00216.

13. Shui, J., Chen, C., Grabstanowicz, L., Zhao, D., and Liu, D.J. (2015). Highly efficient nonprecious metal catalyst prepared with metal-organic framework in a continuous carbon nanofibrous network. Proc. Natl. Acad. Sci. USA *112*, 10629–10634. https://doi.org/10.1073/pnas.1507159112.

14. Chung, H.T., Cullen, D.A., Higgins, D., Sneed, B.T., Holby, E.F., More, K.L., and Zelenay, P. (2017). Direct atomic-level insight into the active sites of a high-performance PGM-free ORR catalyst. Science *357*, 479–484. https://doi.org/10.1126/science.aan2255.

15. Shao, Y., Dodelet, J.P., Wu, G., and Zelenay, P. (2019). PGM-free cathode catalysts for PEM fuel cells: a mini-review on stability challenges. Adv. Mater. *31*, e1807615. https://doi.org/10.1002/adma.201807615.

16. Banham, D., Kishimoto, T., Zhou, Y., Sato, T., Bai, K., Ozaki, J.-i., Imashiro, Y., and Ye, S. (2018). Critical advancements in achieving high power and stable nonprecious metal catalyst–based MEAs for real-world proton exchange membrane fuel cell applications. Sci. Adv. *4*, eaar7180. https://doi.org/10.1126/sciadv.aar7180.

17. Hanif, S., Shi, X., Iqbal, N., Noor, T., Anwar, R., and Kannan, A.M. (2019). ZIF derived PtNiCo/NC cathode catalyst for proton exchange membrane fuel cell. Appl. Catal. B Environ. *258*, 117947. https://doi.org/10.1016/j.apcatb.2019.117947.

18. Wang, C., Kuai, L., Cao, W., Singh, H., Zakharov, A., Niu, Y., Sun, H., and Geng, B. (2021). Highly dispersed Cu atoms in MOF-derived N-doped porous carbon inducing Pt loads for superior oxygen reduction and hydrogen evolution. Chem. Eng. J. *426*, 130749. https://doi.org/10.1016/j.cej.2021.130749.

19. Lim, S.Y., Martin, S., Gao, G., Dou, Y., Simonsen, S.B., Jensen, J.O., Li, Q., Norrman, K., Jing, S., and Zhang, W. (2020). Self-standing nanofiber electrodes with Pt–Co derived from electrospun zeolitic imidazolate framework for high temperature PEM fuel cells. Adv. Funct. Mater. *31*, 2006771. https://doi.org/10.1002/adfm.202006771.

20. Shi, X., and Huang, T. (2015). Effect of pore-size distribution in cathodic gas diffusion layers on the electricity generation of microbial fuel cells (MFCs). RSC Adv. *5*, 102555–102559. https://doi.org/10.1039/c5ra19811a.

21. Li, J., Brüller, S., Sabarirajan, D.C., Ranjbar-Sahraie, N., Sougrati, M.T., Cavaliere, S., Jones, D., Zenyuk, I.V., Zitolo, A., Jaouen, F., et al. (2019). Designing the 3D architecture of PGM-free cathodes for H2/air proton exchange membrane fuel cells. ACS Appl. Energy Mater. *2*, 7211–7222.

22. Fan, M., Cui, J., Wu, J., Vajtai, R., Sun, D., and Ajayan, P.M. (2020). Improving the catalytic activity of carbon-supported single atom catalysts by polynary metal or heteroatom doping. Small *16*, 1906782. https://doi.org/10.1002/smll.201906782.

23. Chong, L., Goenaga, G.A., Williams, K., Barkholtz, H.M., Grabstanowicz, L.R., Brooksbank, J.A., Papandrew, A.B., Elzein, R., Schlaf, R., Zawodzinski, T.A., et al. (2016). Investigation of oxygen reduction activity of catalysts derived from Co and Co/Zn methyl-imidazolate frameworks in proton exchange membrane fuel cells. Chemelectrochem *3*, 1541–1545. https://doi.org/10.1002/celc.201600163.

24. Wang, L., Zeng, Z., Gao, W., Maxson, T., Raciti, D., Giroux, M., Pan, X., Wang, C., and Greeley, J. (2019). Tunable intrinsic strain in two-dimensional transition metal electrocatalysts. Science *363*, 870–874. https://doi.org/10.1126/science.aat8051.

25. Zhou, Z., Liu, T., Khan, A.U., and Liu, G. (2019). Block copolymer–based porous carbon fibers. Sci. Adv. *5*, 6852. https://doi.org/10.1126/sciadv.aau6852.

26. Sun, L., and Okada, T. (2001). Studies on interactions between Nafion and organic vapours by quartz crystal microbalance. J. Memb. Sci. *183*, 213–221. https://doi.org/10.1038/s41563-019-0487-0.

27. Ott, S., Orfanidi, A., Schmies, H., Anke, B., Nong, H.N., Hübner, J., Gernert, U., Gliech, M., Lerch, M., and Strasser, P. (2020). Ionomer distribution control in porous carbon-supported catalyst layers for high-power and low Pt-loaded proton exchange membrane fuel cells. Nat. Mater. *19*, 77–85. https://doi.org/10.1016/S0376-7388(00)00585-8.

28. Wang, X., Li, X., Zhang, L., Yoon, Y., Weber, P.K., Wang, H., Guo, J., and Dai, H. (2009). N-doping of graphene through electrothermal reactions with ammonia. Science *324*, 768–771. https://doi.org/10.1126/science.1170335.

29. Lefèvre, M., Proietti, E., Jaouen, F., and Dodelet, J.-P. (2009). Iron-based catalysts with improved oxygen reduction activity in polymer

electrolyte fuel cells. Science *324*, 71–74. https://doi.org/10.1126/science.1170051.

30. Zitolo, A., Ranjbar-Sahraie, N., Mineva, T., Li, J., Jia, Q., Stamatin, S., Harrington, G.F., Lyth, S.M., Krtil, P., Mukerjee, S., et al. (2017). Identification of catalytic sites in cobalt-nitrogen-carbon materials for the oxygen reduction reaction. Nat. Commun. *8*, 957. https://doi.org/10.1038/s41467-017-01100-7.

31. Barron, A.R. (2015). Characterization of graphene by Raman spectroscopy (Physical Methods in Chemistry and Nano Science).

32. Jaouen, F., Lefèvre, M., Dodelet, J.-P., and Cai, M. (2006). Heat-treated Fe/N/C catalysts for O2 electroreduction: are active sites hosted in micropores? J. Phys. Chem. B *110*, 5553–5558.

33. Guo, D., Shibuya, R., Akiba, C., Saji, S., Kondo, T., and Nakamura, J. (2016). Active sites of nitrogen-doped carbon materials for oxygen reduction reaction clarified using model catalysts. Science *351*, 361–365. https://doi.org/10.1126/science.aad0832.

34. Arrigo, R., Hävecker, M., Schlögl, R., and Su, D.S. (2008). Dynamic surface rearrangement and thermal stability of nitrogen functional groups on carbon nanotubes. Chem. Comm. *40*, 4891–4893. https://doi.org/10.1039/B812769G.

35. Hlil, E.K., BaudoingSavois, R., Moraweck, B., and Renouprez, A.J. (1996). X-Ray absorption edges in platinum-based alloys. 2. Influence of ordering and of the nature of the second metal. J. Phys. Chem. *100*, 3102–3107. https://doi.org/10.1021/jp951440t.

36. Yin, P., Yao, T., Wu, Y., Zheng, L., Lin, Y., Liu, W., Ju, H., Zhu, J., Hong, X., Deng, Z., et al. (2016). Single cobalt atoms with precise N-coordination as superior oxygen reduction reaction catalysts. Angew. Chem., Int. Ed. Engl. *55*, 10800–10805. https://doi.org/10.1002/anie.201604802.

37. Sun, T., Zhao, S., Chen, W., Zhai, D., Dong, J., Wang, Y., Zhang, S., Han, A., Gu, L., Yu, R., et al. (2018). Single-atomic cobalt sites embedded in hierarchically ordered porous nitrogen-doped carbon as a superior bifunctional electrocatalyst. Proc. Natl. Acad. Sci. USA *115*, 12692–12697. https://doi.org/10.1073/pnas.1813605115.

38. Moraweck, B., Renouprez, A.J., Hlil, E.K., and Baudoing-Savois, R. (1993). Alloying effects on x-ray absorption edges in nickel-platinum single crystals. J. Phys. Chem. *97*, 4288–4292. https://doi.org/10.1021/j100119a009.

39. Li, J., Sharma, S., Liu, X., Pan, Y.-T., Spendelow, J.S., Chi, M., Jia, Y., Zhang, P., Cullen, D.A., Xi, Z., et al. (2019). Hard-magnet L10-CoPt nanoparticles advance fuel cell catalysis. Joule *3*, 124–135. https://doi.org/10.1016/j.joule.2018.09.016.

40. Han, B., Carlton, C.E., Kongkanand, A., Kukreja, R.S., Theobald, B.R., Gan, L., O'Malley, R., Strasser, P., Wagner, F.T., and Shao-Horn, Y. (2015). Record activity and stability of dealloyed bimetallic catalysts for proton exchange membrane fuel cells. Energy Environ. Sci. *8*, 258–266. https://doi.org/10.1039/c4ee02144d.

41. Steinbach, A. (2014). Annual Merit Review DOE Hydrogen and Fuel Cells and Vehicle Technologies Programs. http://www.hydrogen.energy.gov/pdfs/review14/fc104_steinbach_2014_o.pdf.

42. Popov, B.N. (2014). Annual Merit Review DOE Hydrogen and Fuel Cells and Vehicle Technologies Programs. http://www.hydrogen.energy.gov/pdfs/review14/fc088_popov_2014_o.pdf.

43. Kongkanand, A. (2018). Annual Merit Review DOE Hydrogen and Fuel Cells and Vehicle Technologies Programs. https://www.hydrogen.energy.gov/pdfs/review18/fc144_kongkanand_2018_o.pdf.

44. Jung, W.S., and Popov, B.N. (2017). New method to synthesize highly active and durable chemically ordered fct-PtCo cathode catalyst for PEMFCs. ACS Appl. Mater. Interfaces *9*, 23679–23686. https://doi.org/10.1021/acsami.7b04750.

45. Zhao, Z., Liu, Z., Zhang, A., Yan, X., Xue, W., Peng, B., Xin, H.L., Pan, X., Duan, X., and Huang, Y. (2022). Graphene-nanopocket-encaged PtCo nanocatalysts for highly durable fuel cell operation under demanding ultralow-Pt-loading conditions. Nat. Nanotechnol. *17*, 968–975. https://doi.org/10.1038/s41565-022-01170-9.

46. Luo, F., Roy, A., Silvioli, L., Cullen, D.A., Zitolo, A., Sougrati, M.T., Oguz, I.C., Mineva, T., Teschner, D., Wagner, S., et al. (2020). P-block single-metal-site tin/nitrogen-doped carbon fuel cell cathode catalyst for oxygen reduction reaction. Nat. Mater. *19*, 1215–1223. https://doi.org/10.1038/s41563-020-0717-5.

47. Qiao, M., Wang, Y., Wang, Q., Hu, G., Mamat, X., Zhang, S., and Wang, S. (2020). Hierarchically ordered porous carbon with atomically dispersed FeN4 for ultraefficient oxygen reduction reaction in proton-exchange membrane fuel cells. Angew. Chem. Int. Ed. Engl. *59*, 2688–2694. https://doi.org/10.1002/anie.201914123.

48. Li, J., Ghoshal, S., Liang, W., Sougrati, M.-T., Jaouen, F., Halevi, B., McKinney, S., McCool, G., Ma, C., Yuan, X., et al. (2016). Structural and mechanistic basis for the high activity of Fe–N–C catalysts toward oxygen reduction. Energy Environ. Sci. *9*, 2418–2432. https://doi.org/10.1039/c6ee01160h.

49. Risch, M., Khare, V., Zaharieva, I., Gerencser, L., Chernev, P., and Dau, H. (2009). Cobalt-Oxo core of a water-oxidizing catalyst film. J. Am. Chem. Soc. *131*, 6936–6937. https://doi.org/10.1021/ja902121f.

50. Risch, M., Klingan, K., Ringleb, F., Chernev, P., Zaharieva, I., Fischer, A., and Dau, H. (2012). Water oxidation by electrodeposited cobalt oxides–role of anions and redox-inert cations in structure and function of the amorphous catalyst. ChemSusChem *5*, 542–549. https://doi.org/10.1002/cssc.201100574.

51. Conway, B.E. (1995). Electrochemical oxide film formation at noble metals as a surface-chemical process. Prog. Surf. Sci. *49*, 331–452. https://doi.org/10.1016/0079-6816(95)00040-6.

52. Poverenov, E., Efremenko, I., Frenkel, A.I., Ben-David, Y., Shimon, L.J.W., Leitus, G., Konstantinovski, L., Martin, J.M.L., and Milstein, D. (2008). Evidence for a terminal Pt(iv)-oxo complex exhibiting diverse reactivity. Nature *455*, 1093–1096. https://doi.org/10.1038/nature07356.

53. Teliska, M., O'Grady, W.E., and Ramaker, D.E. (2005). Determination of O and OH adsorption sites and coverage in situ on Pt electrodes from Pt L_{23} X-ray absorption spectroscopy. J. Phys. Chem. B *109*, 8076–8084. https://doi.org/10.1021/jp0502003.

54. Raciti, D., Kubal, J., Ma, C., Barclay, M., Gonzalez, M., Chi, M., Greeley, J., More, K.L., and Wang, C. (2016). Pt_3Re alloy nanoparticles as electrocatalysts for the oxygen reduction reaction. Nano Energy *20*, 202–211. https://doi.org/10.1016/j.nanoen.2015.12.014.

55. Nilekar, A.U., and Mavrikakis, M. (2008). Improved oxygen reduction reactivity of platinum monolayers on transition metal surfaces. Surf. Sci. *602*, L89–L94. https://doi.org/10.1016/j.susc.2008.05.036.